Experimental and Theoretical Charge Density Study of the Neurotransmitter Taurine

David E. Hibbs,*[a] Charles J. Austin-Woods,[a] James A. Platts,[b] Jacob Overgaard,[a] and Peter Turner[a]

Abstract: The experimental electron density distribution in taurine, 2-aminoethane sulfonic acid, **1**, has been determined from high-resolution X-ray diffraction data collected at a temperature of 100 K. Taurine crystallizes as a zwitterion in the monoclinic space group $P2_1/c$. Topological analysis of the experimental electron density and a comparison with high-level theoretical gas-phase calculations show that the crystal environment has a significant influence on the electronic configuration of the sulfonate moiety in **1**, which in the crystal is more delocalized than in the gas phase. This crystal effect is mainly due to hydrogen bonding.

Keywords: charge density · density functional calculations · hydrogen bonding · taurine · X-ray crystallography

Introduction

Taurine, 2-aminoethane sulfonic acid (**1**, Figure 1), has a variety of functions in the human body. It has a natural role in the development of mammals,[1, 2] with osmoregulatory properties,[3] prevention of lipid peroxidation,[4] and membrane stabilization.[5] Taurine is also a neurotransmitter,[6] an activator and inhibitor of many receptor complexes,[7, 8] and has been shown to competitively bind at the $GABA_A$ receptor.[9, 10] Here, its neurotransmitter properties are largely due to its interaction with receptors located on the neuronal cell body layer and those on the dendrites in the hippocampus.[11] However, it has also been suggested that this is not the only site at which taurine binds.[12] The complementary effects of ethanol and taurine on brain function are of particular current interest given reports that several people have died as a consequence of consuming alcohol in conjunction with certain taurine-containing energy drinks. Such publicity fueled our interest in this molecule, especially as its GABAergic activity is intrinsically involved in the issue. It is known that ethanol has a positive modulatory action on $GABA_A$ receptors,[13] and studies on high-alcohol sensitivity rats suggest that taurine may play a protective role against the adverse effects of alcohol in the central nervous system (CNS), including ethanol-induced sleep time, although it enhances the effect of alcohol at low doses.[14]

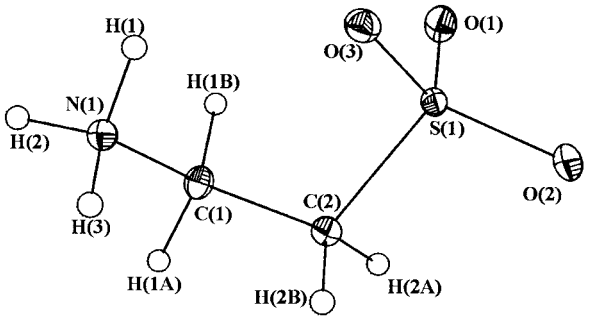

1

Figure 1. Structure of **1** (ORTEP drawing, showing 50% probability ellipsoids).

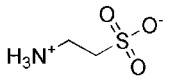

Clearly, taurine is important in a wide range of biochemical processes; it is found throughout the body. These properties ultimately derive from its specific interactions with receptors, lipids, and other biomolecules, which in turn derive from the detailed distribution of electron density within the molecule. For instance, specific polar interactions such as hydrogen bonding and charge–charge interactions play a vital role in protein–ligand docking, and are also known to be important

[a] Dr. D. E. Hibbs, C. J. Austin-Woods, Dr. J. Overgaard, Dr. P. Turner
School of Chemistry
University of Sydney, Sydney, NSW 2006 (Australia)
Fax: (+61) 02 9351 3329
E-mail: d.hibbs@chem.usyd.edu.au

[b] Dr. J. A. Platts
School of Chemistry
Cardiff University, P.O. Box 912, Cardiff, CF1 3TB (Wales)

  0947-6539/03/0905-1075 $ 20.00+.50/0

in determining transport properties such as cell-wall permeability and CNS penetration.[15] We have therefore determined the electron density distribution in taurine using high-resolution X-ray crystallography and theoretical methods, with the aim of understanding the fundamental properties of taurine and how it interacts with its environment.

In addition to the biological aspect, we are interested in taurine because a consistent multipolar description of sulfur in charge density analysis is difficult to obtain. What actually constitutes the best model remains somewhat unclear. Despite the increasing abundance of electron density studies, only relatively few have been devoted to sulfur-containing complexes.[16] One study[16a] has shown that using a modified value of ζ for the sulfur Slater radial function (see Equation (3) below) decreases the overall refinement residual, whereas changing the n_l set was found to have very little influence on the resulting electron density. However, this was before Abramov et al.[17] introduced the concept of the κ''-restricted multipolar model (KRMM), which yielded much more reliable molecular properties such as dipole moments. Taurine is ideal for testing these various conclusions, as it contains charged, zwitterionic groups and a range of bonding motifs, from "simple" σ-C–C and C–N bonds, through hypervalent S=O bonds, to inter- and intramolecular hydrogen bonds.

Experimental Section

X-ray data collection: Crystals of taurine were grown from nonaqueous solvents by slow evaporation. Single-crystal, high-resolution, low-temperature data were collected on a Bruker SMART1000 CCD-based diffractometer. Cell constants were obtained from the least-squares refinement of 4204 reflections located between 2θ values of 5.3 and 106.9°. Three reciprocal space data spheres were collected, with one sphere providing data between 2θ values of 2 and 58°, a second for data between 42 and 98°, and a third for data between 72 and 128°. Data were collected at 100(2) K with ω-scan increments of 0.3°. The intensities of 324 reflections recollected at the end of the experiment did not change significantly during data collection. The data integration and reduction were undertaken with the SAINT+[18] and DREAM[19] suite of programs.

CCDC-195538 contains the supplementary crystallographic data for this paper. These data can be obtained free of charge via www.ccdc.cam.ac.uk/conts/retrieving.html (or from the Cambridge Crystallographic Data Centre, 12 Union Road, Cambridge CB2 1EZ, UK; fax: (+44) 1223–336; or e-mail: deposit@ccdc.cam.ac.uk).

Computational details: All gas-phase DFT calculations were performed with the GAUSSIAN98 package[20] at the 6–311++G** level of theory, using the three-parameter hybrid exchange functional of Becke[21a] in combination (vide supra) with the gradient-corrected exchange-correlation potential of Lee, Yang, and Parr (B3LYP).[21b,c,d] The topological analyses of the theoretical data were based on the wavefunctions obtained from single-point calculations using the same basis sets, and used the AIMPAC suite of programs.[22]

Full optimization of taurine in the gas phase, starting from the experimental geometry, results in transfer of a hydrogen atom from N to O, yielding the neutral, rather than the zwitterionic form. Restricted optimizations, in which the N–H bond lengths were fixed at experimental distances, showed no significant deviations from the crystal structure in bond lengths, angles, or torsions. We therefore report theoretical results only for the experimental geometry, as shown in Figure 1.

Multipole refinement: The aspherical electron density was fitted with a rigid pseudo-atom multipolar description as suggested by Hansen et al.[23] ([Eq. (1) and (2)] and implemented in the XD program package.[24]

In a crystal, the electron density $\rho(\boldsymbol{r})$ can be described by a sum of aspherical pseudoatoms with nuclear positions $\{\boldsymbol{R}_j\}$ as given in Equation (1). It has the pseudoatomic density form of given in Equation (2).

$$\rho(\boldsymbol{r}) = \Sigma_j \rho_j(\boldsymbol{r} - \boldsymbol{R}_j) \quad (1)$$

$$\rho_j(\boldsymbol{r}_j) = P_c \rho_c(\boldsymbol{r}_j) + \kappa'^3 P_v \rho_v(\kappa' \boldsymbol{r}_j) + \sum_{l=1}^{l\max} \sum_{m=0}^{+l} \kappa_l''^3 P_{lm} R_l(\kappa'' \boldsymbol{r}_j) d_{lmp\pm}(\theta_j, \phi_j) \quad (2)$$

The expression for the pseudoatom density includes the usual spherical core, a term to describe the spherical component of the valence density, plus a deformation term describing the asphericity of the valence density. The radial functions $\{R_l(\boldsymbol{r}_j)\}$ are modulated by angular functions $\{d_{lmp}(\theta_j, \phi_j)\}$, defined by axes centered on each atom. A number of radial functions may be used, the most common being Slater-type functions [Eq. (3)].

$$R_l(\boldsymbol{r}) = N r^{n_l} \exp(-\xi_l r) \quad (3)$$

Refinements were carried out using the full-matrix least-squares program XDLSM of XD, while all one-electron properties were determined with XDPROP also part of the XD suite. For all refinements the quantity $\Sigma w |F_{obs}| - K |F_{calcd}|^2$ was minimized with the statistical weight $w = 1/\sigma^2(F_{obs})$, using structure factors that met $F_{obs} > 4\sigma(F_{obs})$. The value of ζ for sulfur was that of the free atom (7.278 Å^{-1}).[25]

An initial high-order independent atom model (IAM) refinement of the structural parameters of the non-hydrogen atoms based on reflections with $\sin(\theta)/\lambda$ values above 0.8 Å^{-1}, where all atoms are treated as spherical, determined the molecular geometry. The N–H and C–H bonds were normalized at 1.009 and 1.092 Å, respectively, corresponding to tabulated neutron diffraction results.[26] Using this structural basis, a κ refinement (HF monopole and κ' only) was carried out. Subsequently, the multipoles were stepwise included in the refinements, ultimately reaching hexadecapoles for S ($l_{max} = 4$), octapoles for O, N, and C ($l_{max} = 3$), while the hydrogen atoms were treated with one monopole and the aspherical density was modeled by a single bond-directed dipole ($l_{max} = 1$). The hydrogen atoms bonded to N, C(1), and C(2), respectively, were treated as chemically independent in all refinements. With this model established, the radial adjustment parameter for the aspherical functions (κ_l'') for each atom type was refined, with the restriction that κ_l'' was the same for all values of l. The values used for the exponents in the expression for the radial functions (n_l) for S were the default values (4,4,4,4,4) for $l = 0-4$. The final model of this form (hereafter denoted model I) was obtained from a subsequent refinement of all parameters, except κ''. The results are summarized in Tables 1 and 2.

It was clear, however, that this model exhibited some discrepancies when compared with the results of the theoretical calculations. In particular, differences were found in the charge density distribution in the sulfur–oxygen bonds, and therefore we concentrated on optimizing our model.

Model optimization: The study of Abramov et al.[17] showed that the use of a kappa-restricted multipolar model in the refinement procedure leads to considerably more reliable molecular properties, in particular dipole moments. The use of a KRMM relates to the problem that might occur with basis set superposition errors for instance in hydrogen bonds, in which very diffuse functions may become necessary to describe the electron density. In a KRMM refinement, the κ_l'' values are fixed as those obtained by multipolar refinement of theoretical structure factors.

KRMM models: The single-point gas-phase calculation based on the experimental geometry was used to generate theoretical structure factors from the DFT wavefunction with same Bragg reflections as used in the experimental refinement. These were free of extinction and anomalous dispersion effects.[27] These data were treated as observations and refined with XDLSM in the same manner as the experimental data. The temperature factors of all atoms were set to zero, since only static Born–Oppenheimer densities are needed for comparison with the static experimental density. The level of multipole expansion in these refinements was identical to the ones used in the refinement against experimental structure factors. Initially, refinement of multipoles and both κ values, was problematic, with κ'' refining to unreasonable values. Thus the values of κ'' were fixed at unity, while refining the multipoles and κ'. Subsequently, all multipoles were fixed and only the κ' and κ_l'' parameters were refined.

0947-6539/03/0905-1076 $ 20.00+.50/0 *Chem. Eur. J.* **2003**, *9*, No. 5

Table 1. Crystallographic details.

empirical formula	$C_2H_7NO_3S$
formula weight [g mol^{-1}]	125.15
crystal system	monoclinic
space group	$P2_1/c$
Z	4
temperature [K]	100
a [Å]	5.2753(2)
b [Å]	11.6569(2)
c [Å]	7.8138(2)
β [°]	93.898(1)
V [Å^3]	479.4
ρ_{calcd} [Mg m^{-3}]	1.734
$F(000)$	264
μ [mm^{-1}]	0.564
crystal size [mm]	0.25x0.20x0.20
wavelength, λ [Å]	0.7107
$[\sin(\theta)/\lambda_{max}]$ [Å^{-1}]	1.24
limiting indices (h, k, l)	−12–11, 0–28, 0–19
number of collected reflections	23424
symmetry-independent reflections	6887
reflections with $F_0 > 4\sigma(F_0)$	6108
completeness	97%
redundancy	av. 5.8
R_{int}	0.023
$R(F)$	0.018
$R(F^2)$	0.026
$R_w(F^2)$	0.035
S	1.66
N_{obs}/N_{var}	30.2

Table 2. Monopole charges and κ values from model I.

Atom	q[P$_v$]	κ'	κ_{1-4}''
S(1)	4.74(4)	1.124(3)	1.008(3)
O(1)	6.87(2)	0.971(1)	0.868(1)
O(2)	6.73(2)	0.971(1)	0.868(1)
O(3)	6.74(2)	0.971(1)	0.868(1)
N(1)	5.51(6)	0.985(3)	0.821(2)
C(1)	3.91(5)	1.025(3)	0.850(2)
C(2)	3.99(4)	1.025(3)	0.850(2)

Atomic positions, scale factor (set to unity) and thermal parameters were not refined.

The κ_l'' values obtained from the refinements of theoretical structure factors (Table 3) were introduced and fixed in the refinement of experimental structure factors. Again, the level of multipole expansion was $l_{max} = 4$ for S and $l_{max} = 3$ for O, C, and N. Besides the multipolar parameters, κ', extinction and scale factors were refined.

It has been shown that second row atoms are often inadequately modeled by the standard n_l-set of (4,4,4,4,4). The coefficients n_l are chosen so that the maximum of the radial function is at the peak density position. Moss and coworkers[28] in an analysis of H_3PO_4, suggested the use of n_l set (6,6,6,7,7) to describe the aspherical density of the phosphorus atom. We adopted this approach with the simplistic reasoning that phosphorus is a close neighbor to sulfur.

Table 3. Monopole and κ values from the least-squares refinements of theoretical structure factors. For κ'', average values are given.

Atom	n_l set (4,4,4,4,4) q[P$_v$]	n_l set (6,6,6,7,7) q[P$_v$]	n_l set (4,4,4,4,4) κ'	κ''	n_l set (6,6,6,7,7) κ'	κ''
S(1)	5.58	5.71	1.005	0.982	1.005	1.033
O(1)	6.23	6.16	0.997	0.995	0.997	1.005
O(2)	6.17	6.02	0.997	0.995	0.997	1.005
O(3)	6.31	6.35	0.997	0.995	0.997	1.005
N(1)	5.62	5.55	0.996	0.965	0.997	0.962
C(1)	4.35	4.36	1.005	0.991	1.004	0.991
C(2)	4.35	4.39	1.005	0.991	1.004	0.991

The refinement details (Table 4) indicate that the default n_l set (4,4,4,4,4) for $l = 0-4$ for S gives the better refinement, although the agreement between theory and experiment seems to be better when the n_l set (6,6,6,7,7) was employed. Therefore, in the following discussion, two KRMM refinements using the (4,4,4,4,4) model (model II) as well as the (6,6,6,7,7) model (model III) will be evaluated. It should be noted that the κ refinement in Table 4 uses the standard n_l-set of (4,4,4,4,4).

Table 4. Selected refinement details.

	κ Refinement[a]	Model II	Model III
$R(F)$	0.023	0.018	0.019
$R(F^2)$	0.037	0.026	0.029
$R_w(F^2)$	0.058	0.035	0.038
S	2.66	1.65	1.76
N_{obs}/N_{var}	78.3	46.3	46.3
κ' (S)	1.122(5)	1.119(3)	1.093(3)
κ' (O)	0.977(1)	0.971(1)	0.975(1)
κ' (N)	1.005(3)	0.988(3)	0.983(2)
κ' (C)	1.042(3)	1.028(3)	1.025(2)

[a] HF monopole and κ' only.

The largest residual density remains in the region close to sulfur as shown by the residual density in the three planes of C(2)-S(1)-O. For model III these are shown in Figure 2 (analogous maps from models I and II are almost identical—see Supporting Information).

Results and and Discussion

Geometric details: The low-resolution structure of **1** has been reported previously.[29] Table 5 details the molecular structure

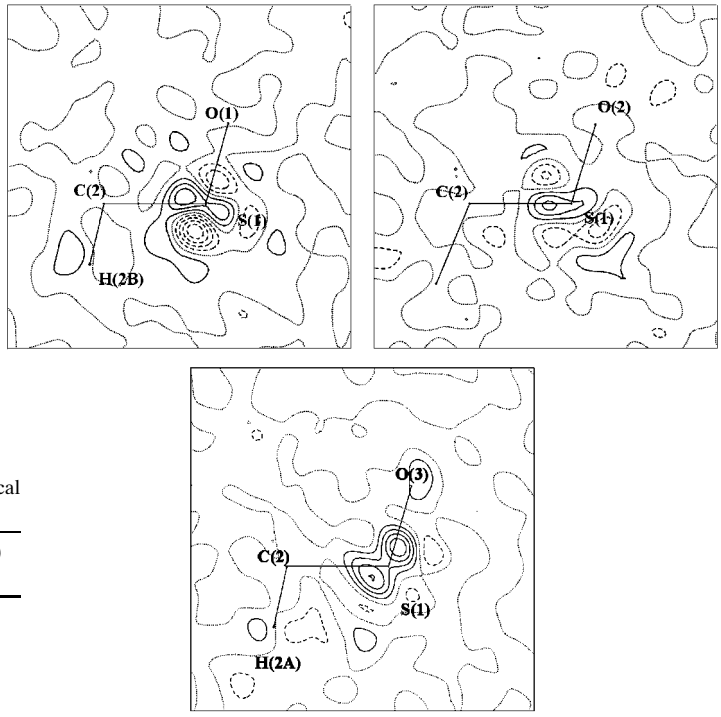

Figure 2. Residual density in the three planes of C(2)-S(1)-O from model III. Solid lines show positive contours, negative contours are dashed. Zero contour is dotted. The contour interval is 0.1 e Å^{-3}.

  0947-6539/03/0905-1077 $ 20.00+.50/0

Table 5. Bond lengths [Å] and angles [°] in **1**.

S(1)–O(1)	1.4720(2)	C(2)-C(1)-N(1)	112.27(2)
S(1)–O(2)	1.4543(2)	O(1)-S(1)-O(2)	113.79(1)
S(1)–O(3)	1.4714(2)	O(1)-S(1)-O(3)	110.85(1)
S(1)–C(2)	1.7858(2)	O(1)-S(1)-C(2)	105.63(1)
C(1)–C(2)	1.5259(3)	O(2)-S(1)-O(3)	113.01(1)
C(1)–N(1)	1.4910(3)	O(2)-S(1)-C(2)	107.01(1)
		O(3)-S(1)-C(2)	105.88(1)
		S(1)-C(2)-C(1)	112.54(2)
		C(2)-C(1)-N(1)	112.27(2)

of **1** as determined in the present experiment. Two of the three S–O bonds (to O(1) and O(3)) have the same length; they are just 0.02 Å longer than the S–O(2) bond. Literature values for the sulfonic acid group[30] show two S=O bonds at 1.42 Å, compared with 1.53 Å for the S–OH bond. The average value for sulfonate S–O bonds is 1.46 Å. Thus, the small differences observed in the experimental S–O bond lengths indicate that almost complete electronic delocalization is present in the SO_3^- region, and hence that no preferential occupation of the extra electron on O(3) is observed in the crystal structure.

It is noteworthy that O(2), while having the shortest S–O bond length, is only involved in very weak hydrogen bonds, whereas the two other oxygen atoms both participate in a much stronger hydrogen bonding pattern (see Table 6). This suggests that hydrogen bonds may influence the degree of electronic delocalization in the SO_3^- group, enhancing the single bond character of bonds to (i.e. negative charge on) the oxygen atoms involved in hydrogen bonds. This will be discussed in greater detail in the topological analysis section.

Electron density distribution in covalent bonds: The electron density distribution (EDD) in the SO_3 region in **1** is illustrated in Figure 3, showing the static deformation density maps in the three C(2)–S(1)–O planes taken from model III. The corresponding plots from models I and II, which have been deposited, show similar features to those in Figure 3. The major difference is that model III gives much lower peak heights around the sulfur atom.

These maps clearly show the bonding density in the C–S and S–O bonds, as well as excess electron density around the oxygen atoms. However, the positions of the maximum deformation density on the O atoms (i.e. lone pair regions) is quite diffuse and does not show any clear pattern. This may be due to the existence of electronic delocalization over all three oxygen atoms, combined with the fact that only the time-averaged situation can be determined with an X-ray diffraction study. In this case, a mix of tetrahedral and planar (sp^3 and sp^2) is expected and the lone pair positions might not reveal any real information. The results of a search for the maxima in the Laplacian of the electron density (the valence shell charge concentrations, or VSCCs) around the oxygen atoms supports this view, since on O(2) and O(3) only two maxima are found, whereas three can be found on O(1). Their geometries are, however, significantly distorted from expected values indicating that these maxima may not correspond to true lone pairs.

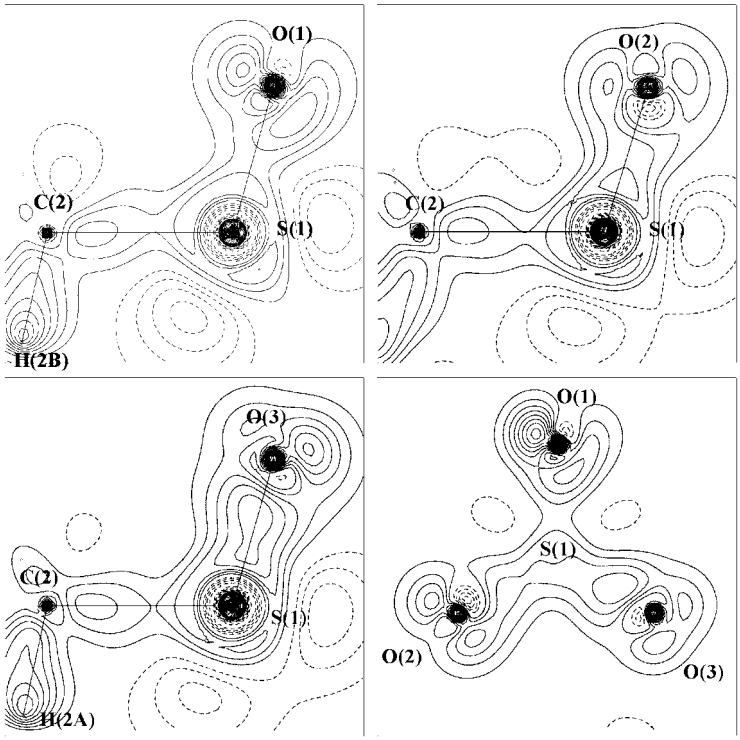

Figure 3. Experimental static deformation density from model III. Contours as in Figure 2.

Table 6. Hydrogen bond geometries.

	Length		Angle
O(1)–H(2)[a]	1.7990(2)	N(1)[a]-H(2)[a]-O(1)	166.18(1)
O(3)–H(3)[b]	1.9219(2)	N(1)[b]-H(3)[b]-O(3)	157.08(1)
O(3)–H(1)[c]	2.2541(2)	N(1)[c]-H(1)[c]-O(3)	129.41(1)
O(3)–H(1)	2.2749(2)	N(1)-H(1)-O(3)	120.79(1)
O(1)–H(1)[c]	2.3682(2)	N(1)[c]-H(1)[c]-O(1)	139.95(1)
O(2)–H(2A)[d]	2.3704(2)	C(2)[d]-H(2A)[d]-O(2)	160.41(1)
O(1)–H(2B)[e]	2.4087(2)	C(2)[e]-H(2B)[e]-O(1)	147.38(1)
O(2)–H(3)[f]	2.4395(2)	N(1)[f]-H(3)[f]-O(2)	108.05(1)

[a] $-x+1, 0.5+y, -z+1.5$. [b] $-x+2, -y, -z+2$. [c] $-x+1, -y, -z+2$. [d] $x, 0.5-y, 0.5+z$. [e] $-x, y, z$. [f] $-x+2, y+0.5, -z+1.5$.

Although there are maxima clearly visible around the oxygen atoms, it remains suspect to assign these maxima as any definitive clear lone pair structure. It is worth noting that model II (Figure 4a) produces S–O bonds, which appear as closed-shell, ionic interactions. This feature can also be recognized in the similar plots from Model I (see Supporting

0947-6539/03/0905-1078 $ 20.00+.50/0 *Chem. Eur. J.* **2003**, *9*, No. 5

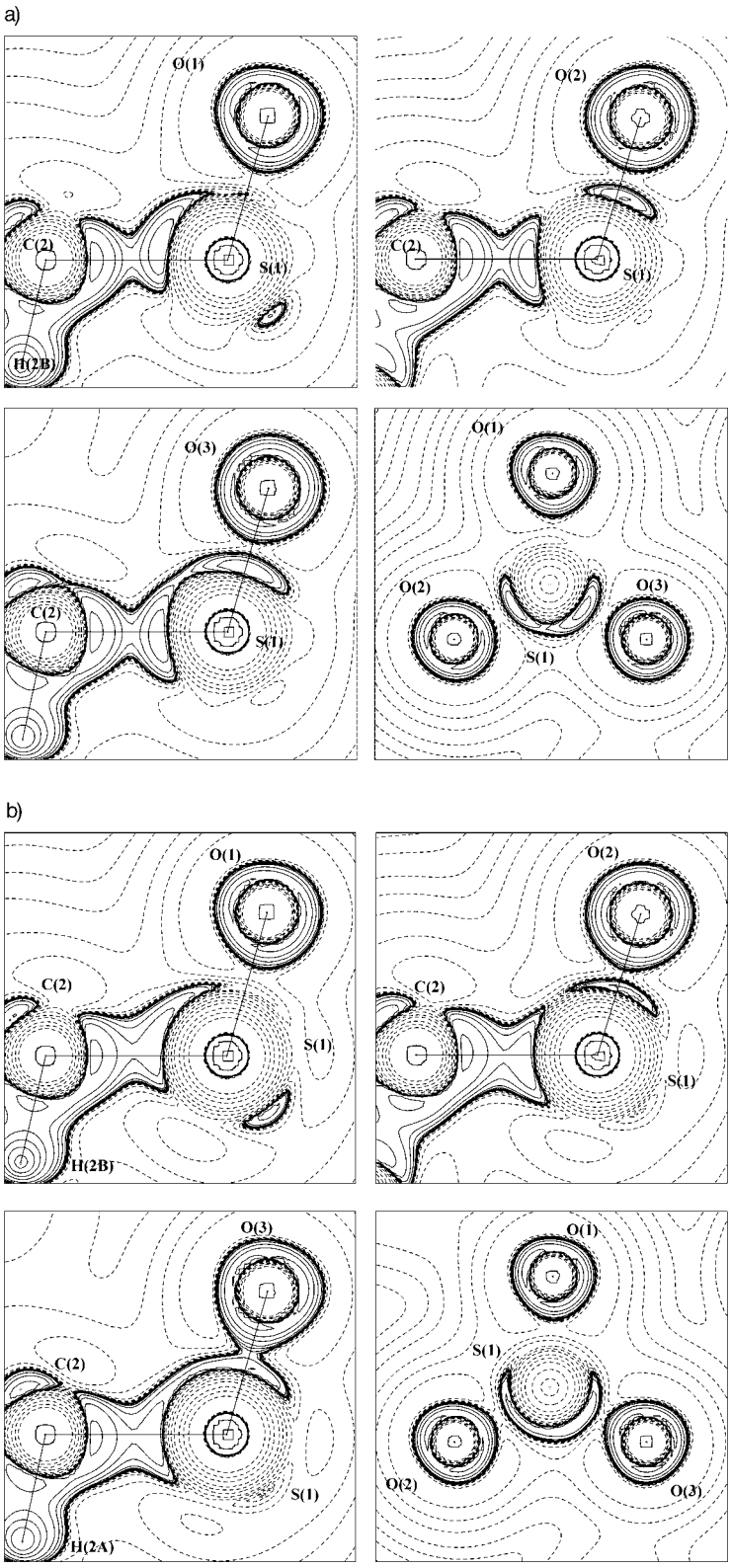

Figure 4. a) Negative Laplacian plots of model II in the same planes as Figure 3. The contours are at 2, 4, and $8 \times 10n$, $n = -2, -1, 0, 1, 2$. Solid lines show positive contours, negative contours are shown with dashed lines. b) Negative Laplacian plots of model III in the same planes as Figure 3.

properties of the S–O bonds will be presented in the next section.

Topological analysis: The theory of atoms in molecules (AIM), developed by Bader and co-workers,[22] makes available a quantitative comparison of bonding features between theory and experiment through the topology of the electron density. Table 7 lists the topological properties of the bond critical points (bcp) in **1**. The degree of similarity between models I and II is extensive, and the results from model I have thus been omitted.

Most topological properties for the majority of bonds show reasonable agreement between experiment and both theoretical models, with high ρ_{bcp}, negative $\nabla^2\rho_{bcp}$, and negligible ellipticity for C–C, S–C, and N–C bonds confirming their single, covalent nature. A general trend is that model II gives bcps that are closer to the oxygen atoms, compared to the theoretical models. The result of using model III is that the bcps are found closer to the sulfur atom, thus closer to the position of the theoretical bcps.

The most significant differences between experiment and theory are found when considering the S–O bonds. Models II and III both show ρ_{bcp} (and hence bond strength) increases from S–O(1) to S–O(3), while theoretical results do not show this trend whatsoever. However, the two models do not agree on the nature of the S–O bonds, as given by the values of $\nabla^2\rho_{bcp}$. In model II, $\nabla^2\rho_{bcp}$ is increasingly negative from S–O(1) to S–O(3), while model III gives very similar and positive values for all three S–O bonds, as do the theoretical results. The value of $\nabla^2\rho_{bcp}$ has been used to label the interatomic interaction as either closed-shell/ionic ($\nabla^2\rho_{bcp} > 0$) or open-shell/covalent ($\nabla^2\rho_{bcp} < 0$),[22] and the two experimental models seem to disagree on this important point.

Information), whereas Model III (Figure 4b) shows an open-shell interaction with O(3). In the theoretical electron density the S–O bonds all appear as open-shell interactions (Figure 5). However, a more elaborate discussion of these

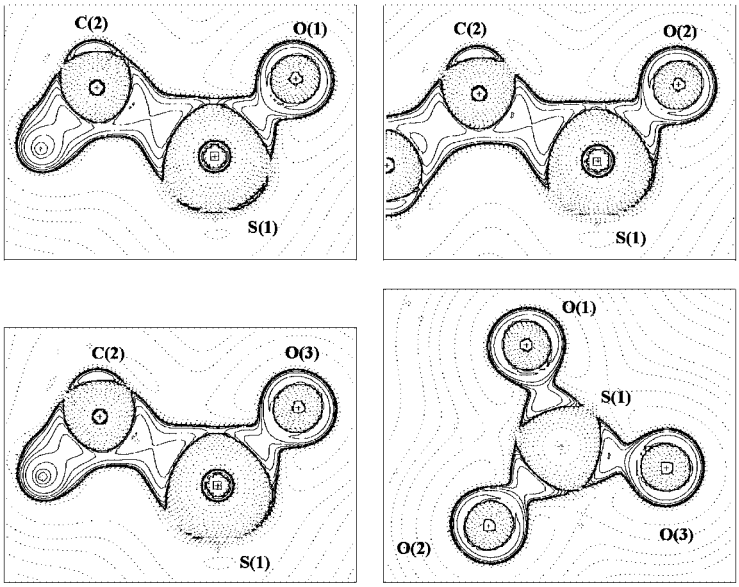

Figure 5. Theoretical negative Laplacian maps. Contours as in Figure 4a.

Table 7. Topological properties at the bond critical points in **1**.

$Bond_{1-2}$	Model	ρ_{bcp} [e Å^{-3}]	$\nabla^2\rho_{bcp}$ [e Å^{-5}]	ε	d_{1-bcp} [Å]	d_{2-bcp} [Å]
S(1)–O(1)	II	1.94(2)	0.08(6)	0.12	0.662	0.810
	III	1.98(2)	3.17(4)	0.06	0.639	0.833
	theory	1.94	20.2	0.03	0.575	0.896
S(1)–O(2)	II	2.28(2)	– 6.89(6)	0.14	0.681	0.774
	III	2.15(1)	3.10(3)	0.11	0.622	0.833
	theory	1.99	24.1	0.03	0.622	0.833
S(1)–O(3)	II	2.47(2)	– 9.36(5)	0.09	0.704	0.768
	III	2.21(1)	2.33(3)	0.07	0.620	0.851
	theory	1.92	21.0	0.02	0.620	0.851
S(1)–C(2)	II	1.26(1)	– 2.42(2)	0.08	0.943	0.843
	III	1.25(2)	– 4.29(3)	0.04	0.919	0.869
	theory	1.41	– 10.2	0.01	0.931	0.856
C(1)–C(2)	II	1.62(2)	– 9.22(3)	0.01	0.792	0.734
	III	1.65(2)	– 9.41(4)	0.02	0.786	0.741
	theory	1.64	– 13.2	0.04	0.799	0.728
N(1)–C(1)	II	1.71(2)	– 9.92(5)	0.10	0.853	0.638
	III	1.73(2)	– 9.73(6)	0.08	0.851	0.641
	theory	1.56	– 11.8	0.03	0.951	0.541

The reason for the large observed discrepancies between theory and experiment can be elucidated by looking at the behavior of ρ and $\nabla^2\rho$ along the interatomic vectors in the three S–O bonds, which are shown in Figure 6 (ρ) and Figure 7 ($\nabla^2\rho$) for models II and III as well as theory. The position of the bcp in the theoretical density is indicated with a vertical line in each plot. These plots give much more elaborate information about the S–O bonds, and show very clearly the difference between the models. It is evident that the curves representing theory and model III have broadly similar appearance, whereas the behavior of $\nabla^2\rho$ in model II is fundamentally different. Thus, the apparently large differences noted in Table 7 between theory and experiment are due to rather small differences in the position of the bcp in these densities, and due to the fact that $\nabla^2\rho$ is changing rapidly in this internuclear region. The explanation for the differences may be the influence of hydrogen bonding, as discussed in the following section. Estimating the values of $\nabla^2\rho$ at the same point, that is the theoretical position of the bcp (shown with a vertical line in Figure 7) gives much better agreement between model III and theory (Table 8). At this distance along the S–O vector, both densities have large, positive $\nabla^2\rho$ values, which might lead us to conclude that these are closed-shell, ionic bonds. Table 8 also confirms that model II differs markedly from these results, since even this close to the S nucleus the S–O(2) bond has a $\nabla^2\rho$ value less than half that found in the other models, and in S–O(3) the Laplacian is actually still negative.

Theoretical calculations allow us to calculate the covalent bond order directly, using the method proposed by Angyan and co-workers.[31] These show bond orders slightly greater than unity for two S–O bonds (1.09, 1.12 to O(1) and O(2), respectively) while the bond to O(3) is calculated to have a covalent order of just 0.97. The slightly lower value for S–O(3) may result from the stronger hydrogen bonding in which this atom is involved (see below), but the overall picture is one of polarized, but still strongly covalent S–O bonds. The homopolar C–C bond has an order of 0.99, while the more heteropolar S–C and N–C bonds have the lower values of 0.76 and 0.87, respectively.

Hydrogen bonding: Table 9 reports the topological properties of the hydrogen bonds identified from model III, and clearly shows that the shortest, strongest hydrogen bond in the system is the intermolecular interaction between O(1) and H(2) (Figure 8). Atom O(3) is involved in intra- and intermolecular hydrogen bonds, of which the intermolecular contact is stronger by a significant margin. The intramolecular contact shows fairly typical hydrogen-bond properties, and although its elipticity is rather high, this value is well within the ranges suggested by Hocquet for stable interactions.[32] Other intermolecular contacts are rather weak, and O(2) has no intermolecular interactions of any significance. By definition, the theoretical EDD includes only the effects of the single intramolecular hydrogen bond between O(3) and H(1), and values calculated here agree well with experimental observations. It is difficult to ascribe the differences observed in S–O bond properties to hydrogen bonding, since on this basis one would expect the best agreement between experiment and theory for O(2) (very weak hydrogen bonds) and the worst for O(1) (strongest hydrogen bond).

Atomic charges: Two definitions of atomic charges, either from refined monopole populations or by integrating the electron density over each atomic basin,[33] are reported in Table 10 for model III and theory. All definitions agree on the broad picture of positive sulfur and negative oxygen and

0947-6539/03/0905-1080 $ 20.00+.50/0 *Chem. Eur. J.* **2003**, *9*, No. 5

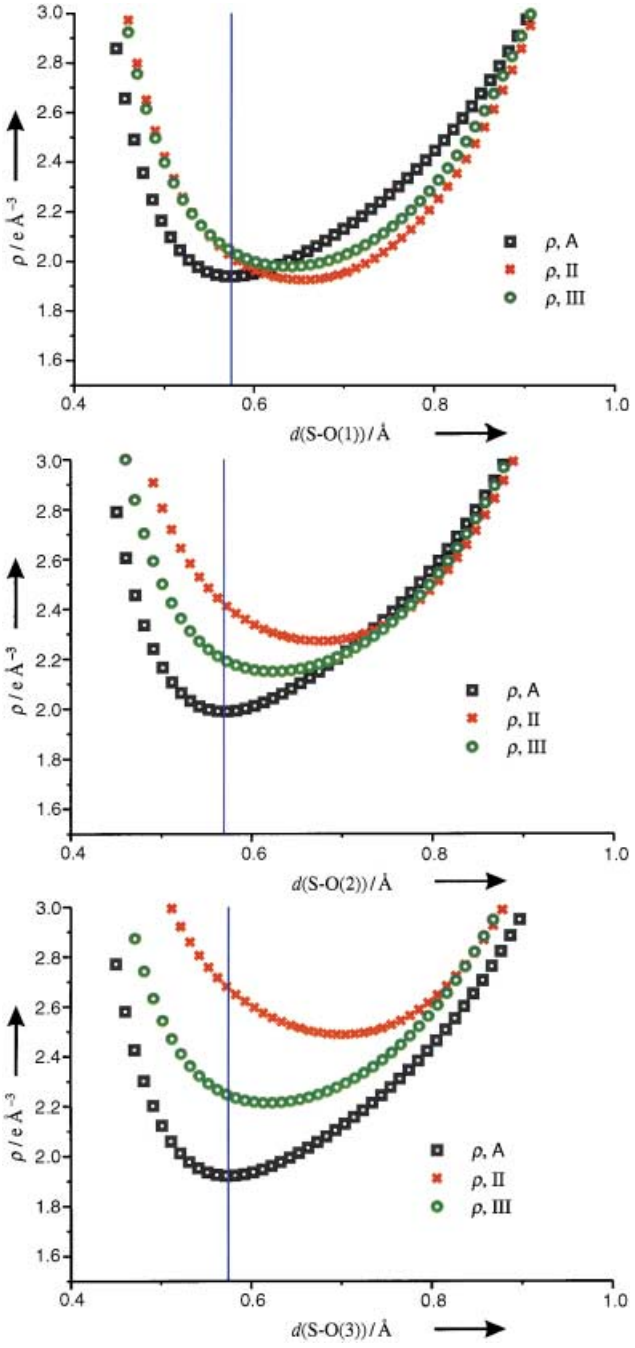

Figure 6. Comparison of the experimental electron density (models II and III) and theoretical electron density along the interatomic S–O lines.

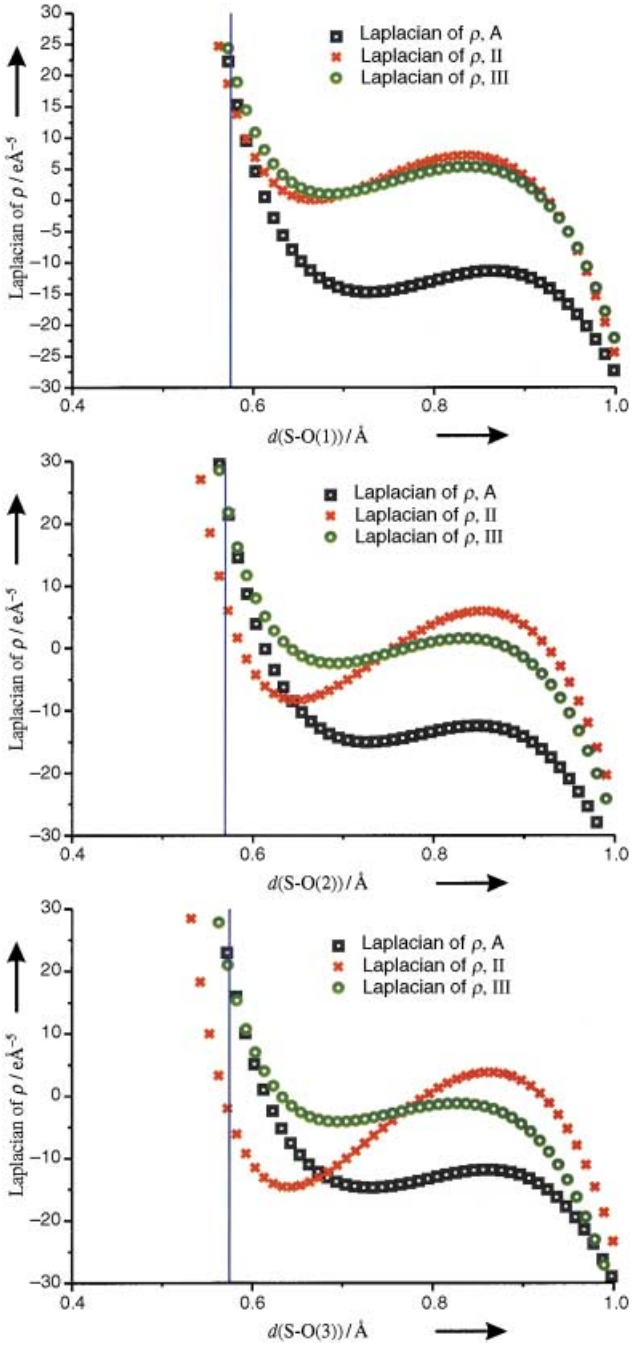

Figure 7. Comparison of the Laplacian of the experimental (models II and III) and theoretical electron density along the interatomic S–O lines.

nitrogen, though the actual values vary considerably within this. We concentrate on the integrated atomic charges here, as these are rigorously derived from the electron density, and can be directly compared between experiment and theory. Notably, charges from the monopolar values from a κ refinement[34] in most cases give the correct sign, but absolute values tend to be significantly underestimated.

The sulfur atom is highly positive, with a charge exceeding +2 electrons. The atomic charges on the oxygen atoms reflect the nearly complete delocalization, though small differences (about 10%) in the charges on O(1) to O(3) are observed in both experimental and theoretical results. The nitrogen atom

Table 8. Bond critical point properties of experimental density at theoretical positions.

$Bond_{1-2}$	Model	ρ_{bcp} [e Å^{-3}]	$\nabla^2\rho_{bcp}$ [e Å^{-5}]
S(1)–O(1)	II	2.02	16.7
	III	2.04	22.2
	theory	1.94	20.2
S(1)–O(2)	II	2.42	7.9
	III	2.20	24.0
	theory	1.99	24.1
S(1)–O(3)	II	2.68	−2.6
	III	2.25	20.2
	theory	1.92	21.0

Table 9. Topological details of hydrogen bonds from model III.

Bond$_{1-2}$	Model	ρ_{bcp} [e Å^{-3}]	$\nabla^2\rho_{bcp}$ [e Å^{-5}]	ε	d_{1-bcp} [Å]	d_{2-bcp} [Å]
O(1)–H(2)[a]	III	0.21(1)	3.65(1)	0.04	1.170	0.631
O(3)–H(3)[b]	III	0.16(1)	2.75(1)	0.01	1.235	0.692
O(3)–H(1)	III	0.10(1)	1.53(1)	0.21	1.322	0.974
	theory	0.11	1.18	0.16	1.412	0.877
O(3)–H(1)[c]	III	0.09(1)	1.46(1)	0.16	1.316	0.960
O(1)–H(1)[c]	III	0.06(1)	1.09(1)	0.72	1.373	1.002
O(2)-H(2A)[d]	III	0.03(1)	0.83(1)	0.84	1.456	1.005
O(1)–H(2B)[e]	III	0.03(1)	0.73(1)	0.55	1.446	1.055
O(2)-H(3)[f]	III	0.07(1)	1.19(1)	0.07	1.345	1.114

[a] $-x+1, 0.5+y, -z+1.5$. [b] $-x+2, -y, -z+2$. [c] $-x+1, -y, -z+2$. [d] $x, 0.5-y, 0.5+z$. [e] $x-1, y, z$. [f] $-x+2, y+0.5, -z+1.5$.

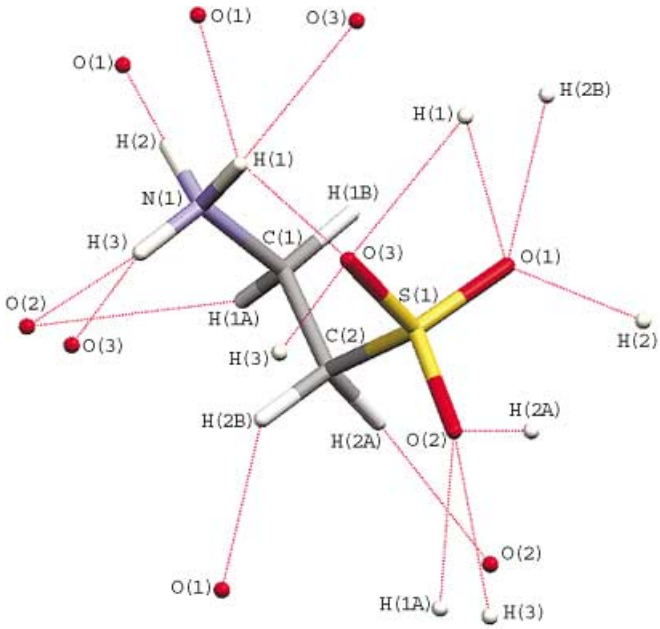

Figure 8. Hydrogen bonding present in taurine.

Table 10. Atomic charges.

Atom	κ-ref q[P$_v$]	Mod III q[P$_v$]	Mod III q[Ω]	Theory q[Ω]	Theory MSK
S(1)	+0.74	+1.62	+2.68	+3.21	+1.36
O(1)	−0.70	−0.78	−1.09	−1.34	−0.68
O(2)	−0.48	−0.62	−1.13	−1.32	−0.65
O(3)	−0.52	−0.73	−1.22	−1.37	−0.73
N(1)	−0.56	−0.37	−1.33	−0.97	−0.48
C(1)	+0.05	+0.01	+0.41	+0.27	+0.17
C(2)	+0.09	−0.21	+0.07	−0.11	−0.50
μ(D)	10.7	15.5	15.5	15.0	15.0

is highly negative, reflecting the fact that it attracts a large amount of electron density from its three hydrogen atoms. However, the NH_3 moiety remains positive when the hydrogen atomic charges are included ($q_{total} = +0.36$). Similarly, the SO_3 group is negatively charged ($q_{total} = -0.97$). The different chemical environment of the two carbon atoms is also reflected in the atomic charges. C(2) is bonded to the highly positive S(1), while C(1) is bonded to the electronegative N(1). The larger positive charge on C(1) is therefore expected.

The molecular dipole moment (Table 10) can easily be calculated from the multipolar parameters, and appears to be very dependent on the choice of radial functions used in the refinements. This dependence can clearly be seen in the comparison of μ from the κ-ref (n_l-set 4,4,4,4,4) and model III (n_l set 6,6,6,7,7). The gas phase dipole moment is 15.0 Debye, while in the crystal environment this ranges from 15.5 D (model III) to 18.0 D (model II) or 18.2 D (model I).

Electrostatic properties of taurine: A useful application of the multipole model is the ability to derive the molecular electrostatic potential (MEP) for an isolated molecule in the crystalline environment, and hence to evaluate contributions of electrostatics to intermolecular interactions and the lattice stabilization.[34] Figure 9a shows the theoretical map as both

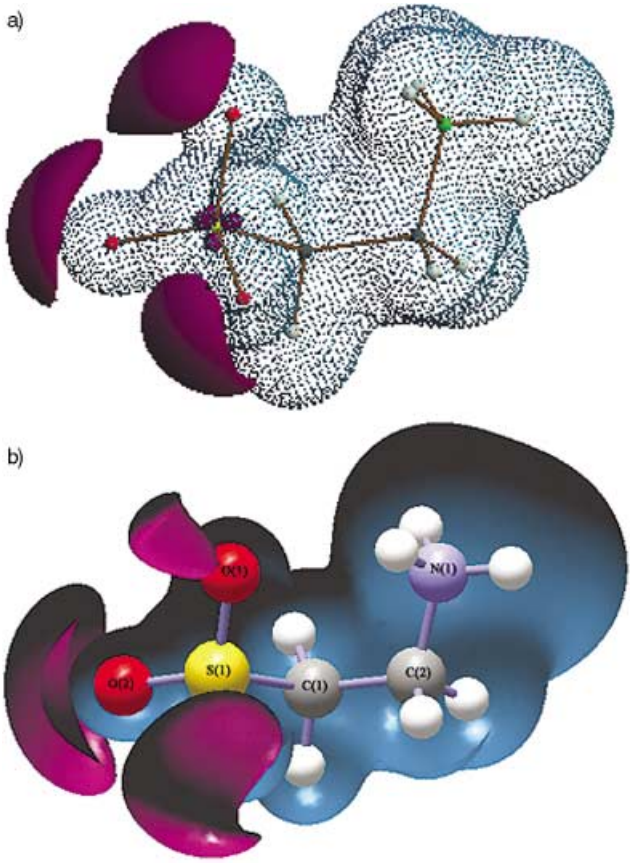

Figure 9. Electrostatic potential around **1** from model III (a) and theory (b).

negative (purple) and positive (blue) regions of this property, at the ± 0.11 au isosurface value. Figure 9b shows the experimental as both negative (purple: -0.2 e Å^{-1}) and positive (blue: $+0.5$ e Å^{-1}) regions of this property of **1**. It is apparent that the negative electrostatic potential is concentrated solely around the SO_3^- group, while the rest of the molecule has positive electrostatic potential, particularly around the NH_3^+ group. This is in accord with the large molecular dipole moment reported in Table 10, which indicates large separation of positive and negative charges.

0947-6539/03/0905-1082 $ 20.00+.50/0 *Chem. Eur. J.* **2003**, *9*, No. 5

Considering first the shape of the theoretical electrostatic potential (Figure 9a), the SO_3^- group is interesting, as it shows substantial differences between O(3), which is involved in the intramolecular hydrogen bond, and the remaining oxygen atoms. The hydrogen bond clearly masks much of the electronegative character of O(3), tying it up in the intramolecular interaction and preventing it from attracting an external positive charge/electrophile. When compared to the experimental MEP this apparent difference is far less pronounced. This can be attributed to the fact that in the crystal all the oxygen atoms are involved in a number of intermolecular hydrogen bonds (not present in the gas-phase calculation), and as a result the MEP has been enhanced over the entire SO_3^- moiety. This distribution of electrostatic potential must have implications for recognition and transport of taurine, since all oxygens and the nitrogen atom are freely available for hydrogen bonding. The oxygen O(3) has a greater negative potential, thus any interactions of this atom will be strengthened by this effect.

The zwitterionic nature of **1** and its correspondingly large dipole moment suggest that electrostatic forces should dominate its intermolecular interactions. The energies of these interactions can be calculated from the set of refined multipoles, which has been shown to give accurate estimates of crystal lattice energies.[35] In the current study, we find that the calculated lattice energy is highly dependent on the choice of multipole model. For model II, a lattice energy of -206.8 (80) kJ mol^{-1} is found, which is reduced to $-121.1(79)$ kJ mol^{-1} using model III. In the former, electrostatic, exchange/repulsion and dispersion forces contribute -369.2, 291.0 and -128.5 kJ mol^{-1}, respectively, while the lower lattice energy in the latter is solely a result of a decrease in the electrostatic contributions by approximately 100 kJ mol^{-1}. Thus, despite the differences between individual models it is evident that electrostatic forces do indeed dominate the intermolecular interactions in crystalline taurine.

The MEP can also be used to derive a set of atomic partial charges, using the Scheme proposed by Mertz et al.[36] These reproduce the potential outside the molecule and hence compactly describe it. Such Mertz–Sing–Kollman (MSK) charges, reported in Table 10, follow the same pattern as those derived from monopole populations or integrated over atomic basins, with negative oxygen and nitrogen atoms and positive sulfur. Unlike in the AIM charges we see that O(2), which has a much smaller electrostatic potential maximum than O(1) and O(3), has a slightly smaller than average MSK charge.

Conclusions

We have determined the high-resolution electron density distribution of taurine using several models based around the standard multipole formalism, and compared the results throughout with the analogous properties determined by theoretical calculation. These studies indicate that the introduction of a κ-restricted multipolar model does not significantly improve the final result, including the molecular moments. On the other hand, a fundamental difference in the interatomic bonds is observed with a change of the radial function employed in the least squares refinements, in contrast to previous studies of the influence of these parameters. Further electron density studies on sulfur-containing complexes are planned to highlight the observed dependence of radial functions of sulfur.

It is noted that topological properties of the electron density alone do not give sufficiently detailed information to compare multipolar models or to obtain an accurate picture of chemical bonding. Instead, detailed study of electron density properties along each internuclear vector is required for the complete picture. This is particularly so in the case of the S–O bonds of the SO_3^- group, which are delocalized and show properties intermediate between single and double bonds such that individual lone pairs cannot be reliably located. The zwitterionic nature of taurine is evident from its electrostatic potential, showing large negative regions around SO_3^- and positive around NH_3^+, with an overall enhancement of the negative potential of the sulfonate group in the crystal environment.

Acknowledgement

We thank the Australian Research Council and the Danish Research Council (J.O.) for funding this work. The Australian Centre for Computing and Advanced Communications (http://www.ac3.com.au) for a generous allocation of computer resources, and the Royal Society of Chemistry for a Journals Grant (J.A.P.).

[1] J. A. Sturman, *Physiol. Rev.* **1993**, *73*, 119–147.
[2] J. M. Hu, J. Y. Rho, M. Suzuki, M. Nishihara, M. Takahashi, *J. Vet. Med. Sci.* **2000**, *62*, 693–698.
[3] R. J. Huxtable, *Physiol. Rev.* **1992**, *72*, 101–163.
[4] I. N. Mankovskaya, T. V. Serebrovskaya, R. J. Swanson, G. L. Vavilova, O. N. Kharlamova, *High Alt. Med. Biol.* **2000**, *1*, 105–110.
[5] P. K. Pokhrel, C. A. Lau-Cam, *Adv. Exp. Med. Biol.* **2000**, *483*, 411–429.
[6] N. del Olmo, J. Bustamente, R. M. del Rio, J. M. Solis, *Brain Res.* **2000**, *864*, 298–307.
[7] A. Dachour, P. De Witte, *Pharmacol. Biochem. Behav.* **2000**, *65*, 345–350.
[8] M. Kurachi, K. Yoshihara, H. Aihara, *Jpn. J. Pharmacol.* **1983**, *33*, 1247–1254.
[9] M. H. Bureau, R. W. Olsen, *Eur. J. Pharmacol.* **1991**, *207*, 9–16.
[10] M. H. Bureau, R. W. Olsen, *J. Neurochem.* **1993**, *61*, 1479–1491.
[11] M. R. Quinn, C. L. Miller, *J. Neurosci. Res.* **1992**, *33*, 136–141.
[12] T. Maar, J. Moran, A. Schousboe, H. Pasantes-Morales, *Int. J. Develop. Neurosci.* **1995**, *13*, 491–502.
[13] M. J. McBroom, A. O. Elkhaward, H. Dlouha, *Gen. Pharmacol.* **1986**, *17*, 97–100.
[14] E. Quetermont, S. Linotte, P. De Witte, *Eur. J. Pharmacol.* **2002**, *444*, 143–150.
[15] *The Application of Charge Density Research to Chemistry and Drug Design* (Eds.: G. A. Jeffery, J. F. Piniella), NATO ASI Series B: Physics *Vol. 250*, Plenum Press, **1991**.
[16] a) E. Espinosa, E. Molins, C. Lecomte, *Phys. Rev. B.* **1997**, *56*, 1820–1833, b) T. W. Hambley, D. E. Hibbs, P. Turner, S. T. Howard, M. B. Hursthouse, *J. Chem. Soc. Perkin Trans. 2* **2002**, 235–239, c) D. Leusser, B. Walfort, D. Stalke, *Angew. Chem.* **2002**, *114*, 2183–2186; *Angew. Chem. Int. Ed.* **2002**, *41*, 2079–2082; d) S. Pillet, M. Souhassou, Y. Pontillon, Y. Caneschi, D. Gatteschi, C. Lecomte, *New J. Chem.* **2001**, *25*, 131–143, e) W. Scherer, M. Spiegler, B. Pedersen, M. Tafipolsky, W. Hieringer, B. Reinhard, A. J. Downs, G. S. McGrady, *Chem. Commun.* **2000**, 635–636, f) K. L. McCormack, P. R.

Mallinson, B. C. Webster, D. S. Yufit, *J. Chem. Soc. Faraday Trans.* **1996**, *92*, 1709 – 1716, g) B. N. Figgis, B. B. Iversen, F. K. Larsen, P. A. Reynolds, *Acta Crystallogr. Sect. B* **1993**, *49*, 794 – 806.
[17] Yu. A. Abramov, A. Volkov, P. Coppens, *Chem. Phys. Lett.* **1999**, *311*, 81 – 86.
[18] Bruker, SMART, SAINT and XPREP. Area detector control, data integration and reduction software. Bruker Analytical X-ray Instruments Inc., Madison, Wisconsin, (USA), **1995**.
[19] R. H. Blessing, *J. Appl. Cryst.* **1997**, *30*, 421 – 426.
[20] M. J. Frisch, G. W. Trucks, H. B. Schlegel, G. E. Scuseria, M. A. Robb, J. R. Cheeseman, V. G. Zakrzewski, J. A. Montgomery, Jr., R. E. Stratmann, J. C. Burant, S. Dapprich, J. M. Millam, A. D. Daniels, K. N. Kudin, M. C. Strain, O. Farkas, J. Tomasi, V. Barone, M. Cossi, R. Cammi, B. Mennucci, C. Pomelli, C. Adamo, S. Clifford, J. Ochterski, G. A. Petersson, P. Y. Ayala, Q. Cui, K. Morokuma, D. K. Malick, A. D. Rabuck, K. Raghavachari, J. B. Foresman, J. Cioslowski, J. V. Ortiz, A. G. Baboul, B. B. Stefanov, G. Liu, A. Liashenko, P. Piskorz, I. Komaromi, R. Gomperts, R. L. Martin, D. J. Fox, T. Keith, M. A. Al-Laham, C. Y. Peng, A. Nanayakkara, C. Gonzalez, M. Challacombe, P. M. W. Gill, B. Johnson, W. Chen, M. W. Wong, J. L. Andres, M. Head-Gordon, E. S. Replogle, J. A. Pople, Gaussian 98, Revision A.7, Gaussian, Inc., Pittsburgh PA, **1998**.
[21] a) A. D. Becke, *J. Chem. Phys.* **1993**, *98,* 5648 – 5652, b) C. Lee, W. Yang, R. G. Parr, *Phys. Rev. B* **1988**, 37, *2*, 785 – 789, c) P. J. Stevens, F. J. Devlin, C. F. Chabalowski, M. J. Frisch, *J. Phys. Chem.* **1994**, *98,* 11 623 – 11 627, d) C. Adamo, V. Barone, *Chem. Phys. Lett*. **1997**, *274*, 242 – 250.
[22] R. F. W. Bader, *Atoms in Molecules a Quantum Theory*, Clarendon Press, Oxford, **1990**.
[23] N. K. Hansen, P. Coppens, *Acta Crystallogr. Sect. A* **1978**, *39*, 909 – 921.
[24] T. Kortisanszky, S. T. Howard, P. R. Mallinson, Z. Su, T. Richter, N. K. Hansen, XD - a computer program package for the multipole refinement and analysis of electron densities from diffraction data. Free University of Berlin, (Germany) **1997**.
[25] E. Clementi, D. L. Raimondi, *J. Chem. Phys.* **1963**, *38*, 2686 – 2689.
[26] F. H. Allen, *Acta Crystallogr. Sect. B* **1986**, *42*, 515 – 522.
[27] S. T. Howard, FSTRUCT, an *ab-initio* one-electron properties program, University of Cardiff, (UK), **1991**.
[28] G. R. Moss, M. Souhassou, R. H. Blessing, E. Espinosa, C. Lecomte, *Acta Crystallogr. Sect. B* **1995**, 51, 650 – 660.
[29] a) H. H. Sutherland, D. W. Young, *Acta Crystallogr.* **1963**, *16*, 897 – 901; b) Y. Okaya, *Acta Crystallogr.* **1966**, *21*, 726 – 735; c) C. E. Bryant, D. W. Jones, *J. Chem. Crystallogr.* **1997**, *27*, 481 – 483, d) C. H. Gorbitz, K. Prydz, S. Ugland, *Acta Crystallogr. Sect. E* **2000**, *56*, 23 – 24.
[30] R. G. Delaplane, J. O. Lundgren, I. Olovsson, *Acta Crystallogr. Sect. B* **1975**, *31*, 2208 – 2213.
[31] J. G. Ángyán, E. Rosta, P. R. Surján, *Chem. Phys. Lett*. **1999**, *299*, 1 – 8.
[32] A. Hocquet, *Phys. Chem. Chem. Phys.* **2001**, *3*, *15*, 3192 – 3199.
[33] A. Volkov, C. Gatti, Yu. Abramov, P. Coppens, P. *Acta Crystallogr. Sect. A* **2000**, *56*, 252 – 258.
[34] P. Coppens, *X-Ray Charge Densities and Chemical Bonding*, Oxford University Press: Oxford, **1997**.
[35] Yu. A. Abramov, A. Volkov, G. Wu, P. Coppens, *Acta Crystallogr. Sect. A* **2000**, *56*, 585 – 591.
[36] a) U. C. Sing, P. A. Kollman, *J. Comput. Chem.* **1984**, *5*, 129 – 145; b) B. H. Bezler, K. M. Mertz, P. A. Kollman, *J. Comput. Chem.* **1990**, *11*, 431 – 439.

Received: October 18, 2002 [F4512]

  0947-6539/03/0905-1084 $ 20.00+.50/0